Simulating Thermal Wood Particle Conversion: Ash-Layer Modeling and Parametric Studies

Inge Haberle,[*,†] Nils Erland L. Haugen,[*,†,‡] and Øyvind Skreiberg[‡]

[†]Department of Energy and Process Engineering, Norwegian University of Science and Technology, Kolbjørn Hejes vei 1 B, 7491 Trondheim, Norway

[‡]Department of Thermal Energy, SINTEF Energy Research, Kolbjørn Hejes vei 1 A, 7491 Trondheim, Norway

ABSTRACT: In this work, we study the thermochemical degradation and char conversion of wet wood particles. The work is split in two main parts: (1) the effect of the ash layer handling approach and (2) a parametric study over different relevant parameters. In the study of the ash layer handling, we investigate the effect of allowing the ash to remain on the surface of the particle when the char is converted (Model A), in contrast to removing the ash such that the reacting char layer is always exposed (Model B). It was found that the two modeling concepts yield significantly different mass losses and surface and center temperature predictions. Model B presents a faster thermal conversion, while the results predicted by Model A are in better agreement with what has been observed experimentally. A parametric study was also done, where the sensitivity to variations in thermal conductivity, specific surface area, and gas permeability was studied. It was found that thermal conductivity influences the time when drying and devolatilization are accomplished. This is because these conversion stages are heat-transfer-controlled. Char conversion is primarily affected by a shift to earlier times for the initialization of the final char conversion when higher thermal conductivities are used. It is found that the specific surface area smaller than a critical value can significantly affect the final char conversion time. Since char conversion is a key stage of wood combustion, the full conversion time is also affected. The gas permeability primarily affects mass diffusion into the particle. It was found that, up until a critical effective gas permeability, the modeling results are sensitive to assigned permeabilities.

1. INTRODUCTION

Wood combustion is currently a main field of research. The increased focus on wood combustion is due to the renewable character of wood as an energy source. In order to understand chemical and physical phenomena related to wood combustion, numerical modeling has proven to be a useful tool. Hence, over the last decades, many fundamental studies on thermochemical wood degradation and combustion have been performed by the use of numerical simulation tools.[1]

Different models for wood combustion are available, with most of them being one-dimensional (1D).[2−8] Such 1D models allow for fundamental studies of combustion-related processes while, at the same time, remaining numerically efficient.

One important element of a model describing drying, devolatilization, and char conversion is the structural change due to volumetric shrinkage and char conversion. This change in particle size can have an influence on the thermochemical degradation of the particle.[9]

However, generally, note that shrinkage is a multidimensional phenomenon that is always simplified in 1D models. The multidimensional character of shrinkage has been experimentally observed by Grønli.[10] While shrinkage during drying is commonly neglected, since it is only small, compared to shrinkage during devolatilization,[2] the volumetric shrinkage during devolatilization must be taken into account, because of significant organic mass loss during devolatilization. This volumetric shrinkage is often modeled by empirical shrinkage factors.[4] However, most challenging is the enormous size reduction that affects the particle during char conversion. It is

still studied how this size reduction can be accurately predicted by 1D models. Since char is consumed by gasification and oxidation, the particle size is significantly decreasing. The final size of the particle can be predicted differently in models by either neglecting or considering residual ash in the model.

Wood is a biomass source with low ash content, which suggests that an ash layer could potentially be neglected in a combustion model, because of its negligible influence on heat and mass transfer. However, reviewing earlier works on wood combustion modeling shows that a common modeling assumption is to consider an up-building ash layer and especially its effect on heat and mass transfer.[3,4] An advantage of this modeling assumption is that the boundaries are fixed to the same grid point during drying, devolatilization, and char conversion. This implies that the char conversion front does not have to be tracked. This modeling assumption predicts the mass loss well, when validated against experiments. At the same time, it shows that the predicted surface and center temperatures are different from experimental measurements.[3,4] Even though the deviation between modeling results and experiments can also be due to inaccurate temperature measurements, because of the significant size reduction of the particle during char conversion, it might as well be due to an inadequate handling of the ash layer. The ash layer also affects the oxygen diffusion to the char surface, which has an impact on the modeling results. This consideration of diffusion

through an up-building ash layer can be conducted differently based on the choice of ash porosity. It can even be fully neglected by assuming the absence of the ash (i.e.; the ash is immediately removed from the surface after full char conversion at a distinct location). One might assume that the suitability of the two modeling approaches is linked to the experimental conditions as well as the ash chemistry. The ash chemistry of a sample can affect the importance of the ash layer, with respect to heat and mass transfer, and also catalytic effects of the ash on conversion chemistry, as will be discussed in the following section. One might expect that, for agricultural biomass, ash chemistry becomes crucial, since the composition of ash can cause an encapsulation of the unreacted char, because of low ash melting temperatures. For those types of biomass, one might expect that the consideration of the ash layer, with respect to heat and mass transfer, will significantly affect the char conversion time. On the other hand, for ash obtained when converting a woody fuel with low ash content, ash melting is not a major concern, and the ash structure is not altered by increasing temperatures, such that heat and mass transfer are not expected to be significantly altered. The ash maintains a porous structure.[11] For woody biomass, therefore, one would rather expect that, by purely judging ash chemistry, the consideration of the ash layer is of negligible importance if the ash content is minor and the ash is highly porous. This is, indeed, also what Strandberg et al.[11] stated, who found that, generally, char conversion rates could be affected by dense ash layers (which themselves are often dominated by low-temperature melting alkali silicates). However, such an inhibition is unlikely to occur for woody-type biomass, since woody biomass ash has a high content of calcium and low silicon content, resulting in higher ash melting temperatures.[11] It shall be noted that the consideration of the presence or absence of an ash layer might also be a function of whether or not the bark layer surrounding the stem wood is modeled or not. Bark and stem wood have significantly different ash fractions and the ash chemistry can also differ significantly. Also, experimental conditions can have an impact on the validity of the two modeling approaches for certain test cases. Therefore, one can already observe that the motivations for the applicability of the two models is very vast and can be a field of research just by itself.

Therefore, this work focuses on how the different modeling concepts—with one considering an up-building ash layer and one neglecting it—affect the model predictions for thermal conversion times and particle temperatures. To the authors' knowledge, such a comparison of combustion models with fixed boundary conditions and inward-moving boundary conditions has not been done previously.

In addition, the model's sensitivity to the specific surface area of char and thermal conductivities of char and wood was also studied. The thermal conductivity is assumed to mainly affect drying and devolatilization, both being heat-transfer-controlled conversion stages, while the specific surface area is assumed to affect the char conversion modeling results, since it alters the reactivity of the char. Furthermore, the sensitivity of the model to gas permeability was also tested.

1.1. Ash Contents of Hardwoods and Softwoods.
Compared to other types of biomass, e.g., rice straw (ash fraction of 19.2% dry basis),[12] wood has a very low ash content (see Table 1).

Table 1 shows that the majority of the wood species has an ash fraction of <0.5 wt % (dry basis). Because of the very low

Table 1. Ash Contents of Different Wood Species[a]

wood species[b]	hardwood	softwood	ash content (%, dry basis)
maple	√		0.3667
American beech	√		0.4
hickory	√		0.75
oak	√		0.6
pine		√	0.29
birch	√		0.5
yellow poplar	√		1
basswood	√		0.4
fir		√	0.383
hemlock		√	0.467
cedar		√	0.367
spruce		√	0.267

[a]All original data has been taken from the work of Pettersen,[13] but averaging according to species has been done by the authors. [b]Checkmarks (√) indicate that the wood species written in bold have been averaged, since different subspecies of the wood species have been tested and different ash fractions were measured.

ash content, the authors assumed that the development of a model where the ash "falls off" during char conversion, because of its negligible influence on heat and mass transfer, could be an alternative modeling approach, compared to most of the already-existing wood degradation models (see, e.g., refs 4 and 14). It is of interest to then study if the results of this modeling approach can get closer to experimental data. The "falling off" of the ash layer purely refers to the negligence of the ash layer in the numerical model, because of assumingly negligible influence of the ash layer on heat and mass transfer. In a numerical model, the "falling off" of the ash layer can be implemented by inward moving boundary conditions that are fixed to the outer char conversion front. Instead, an explicit consideration of the ash layer is taken into consideration by fixed boundary conditions.

1.2. Theory of Char Reactivity.
An accurate description of the char conversion stage is a key element of any simulation tool that will be used for design and optimization of combustion or gasification technologies. The reason is that char conversion (oxidation and gasification) can be the limiting stage of the entire conversion under certain conditions.[15]

The accuracy of a model is not only dependent on the modeling approach (fixed or inward-moving boundaries) but also on input data, such as specific surface area. Even though the char conversion of thermally thick wood particles is diffusion-controlled, it is also of interest to study how sensitive the model accuracy is to the input data describing char reactivity. Char reactivity is influenced by the following properties:[15]

(1) Surface area that can be accessed and is therefore available for surface reactions.

(2) The inorganic compounds that are found in the carbon skeleton of the char and, consequently, also the concentration at which the inorganic matter is present.

(3) The type of functional groups in the char and the concentration of those groups.

Those properties are influenced by the initial wood properties as well as the devolatilization process under which the char is formed.[15] In this work, the model's sensitivity to char reactivity is tested by means of specific surface area.

Table 2. Experimentally Measured Specific Surface Areas of Different Wood Chars Obtained under Different Conditions[a]

ref	wood char species	temperature, T_{pyro} (°C)	moisture (%)	measurement	SSA (m² m⁻³)
Lu et al.[4]	poplar	NA	NA	BET	1×10^6
Grønli[10]	birch	NA	NA	b	4.1×10^7
Grønli[10]	spruce	NA	NA	b	4.59×10^7
Burhenne et al.[16]	spruce	500	2.4% (w.b.)	BET (N₂)	1.96×10^7
Burhenne et al.[16]	spruce	500	16.4% (w.b.)	BET (N₂)	3.97×10^7
Burhenne et al.[16]	spruce	500	55.4% (w.b.)	BET (N₂)	3.75×10^7
Burhenne et al.[16]	spruce	800	2.4% (w.b.)	BET (N₂)	5×10^2
Burhenne et al.[16]	spruce	800	16.4% (w.b.)	BET (N₂)	1.669×10^5
Burhenne et al.[16]	spruce	800	55.4% (w.b.)	BET (N₂)	1.066×10^5
Link et al.[17]	Douglas fir	800	6.47% (d.b.)	BET (N₂)	3.16×10^7
Link et al.[17]	Douglas fir	800	6.47% (d.b.)	BET (CO₂)	3.98×10^7
Link et al.[17]	pine	800	8.6% (d.b.)	BET (N₂)	4.85×10^7
Link et al.[17]	pine	800	8.6% (d.b.)	BET (CO₂)	5.36×10^7
Anca-Couce et al.[15]	pine	500	NA[c]	BET (N₂)	1.5176×10^6
Anca-Couce et al.[15]	pine	500	NA[d]	BET (N₂)	2.120×10^5
Anca-Couce et al.[15]	pine	500	NA[d]	BET (N₂)	1.06095×10^7

[a]Here, d.b. refers to the dry basis and T_{pyro} is the peak temperature at which the pyrolysis was accomplished. The abbreviation SSA is used to denote specific surface area, while BET refers to the "Brunauer−Emmett−Teller" testing method to define the total specific surface area. The specific surface area is given in units of m² m⁻³ (if the original data were given in units of m² g⁻¹, this has been converted by using an assumed apparent char density of 100 kg m⁻³). [b]A Coulter SA 3100 Surface Area Analyzer has been used to measure the specific surface area. [c]Anca-Couce et al.[15] produced the tested chars with TGA. More information regarding this can be found in their work. [d]Anca-Couce et al.[15] produced the tested chars in a fixed-bed reactor. More information regarding this can be found in their work.

In Table 2, measured specific surface areas for wood chars are presented. It is obvious that the observed values spread over a large range.

Char formed under lower temperatures has a low specific surface area. However, the final surface area is not dependent on the temperature alone.[18]

By evaluating the data in Table 2, it turns out that there is a significant scattering in the measured char surface areas. One main reason for this is that the measurement methods can vary and, based on this variation, significantly different specific surface areas can be determined for the same char (e.g., comparing the specific surface areas obtained with BET measurements with N₂ or CO₂ in Table 2).

Nitrogen is typically used for BET measurements, but note that the corresponding results can be affected by diffusion limitations of the gas into micropores. Based on this, the surface area might be underestimated. This limitation is the motivation for why some BET measurements are performed with CO₂, because it diffuses more easily into fine pores and therefore predicts a higher specific surface area. The restrictions of BET measurements performed with nitrogen have been reported to range from being significant to even not being able to measure the specific surface area of biochars generated at low-temperature conditions at all, while BET measurements performed with CO₂ were able to measure specific surface areas in the range of hundreds of m² g⁻¹.[18]

Furthermore, note that the measured specific surface area as such is not necessarily equal to the specific surface area accessible for heterogeneous char reactions. This is due to the distinct groups of pores, namely, macropores (>50 nm diameter), mesopores (2−50 nm diameter), and micropores (<2 nm diameter), which are affecting the measured inner specific surface area (of course, the influence on micropores is dependent on the testing gas used in BET measurements). However, heterogeneous char reactions occur primarily in macropores and mesopores, even though the micropores will significantly increase the measured surface area.

The influence of the total specific surface area, $s_{a,char}$, in common comprehensive combustion models enters in a simplified manner:[4]

$$\dot{\omega}_i = s_{a,char}\left(\frac{\rho_{char}}{\rho_{char} + \rho_{wood} + \rho_{ash}}\right)k_i\rho_{g,k}$$

(1)

with k_i being the reaction rate constant and $\rho_{g,k}$ being the phase-averaged species gas density of the reacting gas species k (either O₂, CO₂ or H₂O). The sensitivity of the model to the input data for $s_{a,char}$ can be studied. The input data for specific surface area equals measured BET surface data. The deactivation of active sites due to reduced char density is considered by the term $\frac{\rho_{char}}{\rho_{char} + \rho_{wood} + \rho_{ash}}$. Active sites refer to carbon edges, oxygen-containing functional groups, and inorganic impurities, onto which the reacting gas can chemisorb through electron transfer.[18] Based on the range of experimental data available for specific surface areas, it is of interest to investigate how much the variation of measured specific surface area can affect the modeling results.

1.3. Thermal Conductivities of Wood and Char. In the same way as there is a significant scattering in existing data on specific surface area, a wide range of thermal conductivities for wood and char is also found in the literature.[1] Since both drying and devolatilization are controlled by the internal heat transfer, the choice of char and wood thermal conductivity will affect the wood particle conversion time. The study of the significance of this influence is part of this work.

1.4. Gas Permeabilities. Modeling input data that can be directly linked to the gas phase flow, such as gas permeabilities, scatter significantly.[1] Values can differ significantly for different wood species.[10] Also, with respect to char permeability, different data can be found.[1] Char permeabilities are larger than wood permeabilities, because of pore enlargement during conversion. Because of this scattering in data, the authors studied how the choice of gas permeability affects the temperature history and normalized residual mass.

Table 3. List of Evolution Equations for Drying, Devolatilization, and Char Conversion[a]

	evolution equation	equation number	ref
wood density[b]	$\frac{\partial \rho_{\text{wood}}}{\partial t} = -(k_1 + k_2 + k_3)\rho_{\text{wood}} - \frac{\rho_{\text{wood}}}{V_j}\frac{\partial V_j}{\partial t}$	(2)	4
ash density	$\frac{\partial \rho_{\text{ash}}}{\partial t} = -\frac{\rho_{\text{ash}}}{V_j}\frac{\partial V_j}{\partial t}$	(3)	4
continuity equation	$\frac{\partial \epsilon_g \rho_g^g}{\partial t} + \frac{1}{r}\frac{\partial}{\partial r}(r\rho_g^g u_r) = \dot{\omega}_g$	(4)	4
species mass fraction	$\frac{\partial (\epsilon_g \rho_g^g Y_k)}{\partial t} + \frac{1}{r}\frac{\partial (r\rho_g^g Y_k u_r)}{\partial r} = \frac{1}{r}\frac{\partial}{\partial r}\left(r\rho_g^g D_{\text{eff}}\frac{\partial Y_k}{\partial r}\right) + \dot{\omega}_k$	(5)	4
char density[c]	$\frac{\partial \rho_{\text{char}}}{\partial t} = k_3\rho_{\text{wood}} + \epsilon_g k_5\rho_{\text{tar}}^g - \frac{\rho_{\text{char}}}{V_j}\frac{\partial V_j}{\partial t} - \dot{\omega}_{\text{oxid}}\frac{2\text{MW}_C}{\text{MW}_{O_2}} - \dot{\omega}_{\text{steam,gasif}}\frac{\text{MW}_C}{\text{MW}_{H_2O}}$ $- \dot{\omega}_{\text{CO}_2,\text{gasif}}\frac{\text{MW}_C}{\text{MW}_{\text{CO}_2}}$	(6)	4
temperature	$(\rho_{\text{wood}}c_{P,\text{wood}} + \rho_{\text{ash}}c_{P,\text{ash}} + \rho_{\text{char}}c_{P,\text{char}} + \rho_b c_{P,b} + \epsilon_g \rho_g^g c_{P,g})\frac{\partial T}{\partial t} + (\rho_g^g c_{P,g} u_r)\frac{\partial T}{\partial r}$ $= \frac{1}{r}\frac{\partial}{\partial r}\left(r\lambda_{\text{eff}}\left(\frac{\partial T}{\partial r}\right)\right) + \Phi_{\text{Heat}}$	(7)	14
bound water[d]	$\frac{\partial \rho_b}{\partial t} = \frac{1}{r}\frac{\partial}{\partial r}\left(rD_b\frac{\partial \rho_b}{\partial r}\right) - k_{\text{evap,b}}\rho_b$	(8)	10

[a]The last column gives the references from which the equations have been taken. [b]The reaction rates of wood to noncondensable gases, tar, and char are given by k_1, k_2, and k_3, respectively. [c]k_5 marks the reactions of tar to char. [d]$k_{\text{evap,b}}$ is the kinetic evaporation rate constant for bound water.

2. NUMERICAL MODEL

A detailed discussion of the drying and devolatilization model for thermally thick wood particles that is applied here can also be found in earlier works.[19] There is literature available that discusses the applied governing equations for the entire wood particle combustion in much detail (see, e.g., refs 3, 4, 14, and 20); however, for the sake of completeness, we list them in Table 3. In this work, all the water (liquid + bound) is treated as bound water and drying is therefore modeled by the kinetic rate drying model. The reaction rates that appear in some of the governing equations in Table 3 are listed in Table 4. The source terms for devolatilization and char conversion have been modeled as suggested by Lu et al.[4]

The heat source term (Φ_{heat}) in Table 3 is defined as

$$\Phi_{\text{heat}} = \dot{\omega}_{k_1,k_2,k_3}\Delta h_{\text{devol,1}} + \dot{\omega}_{k_4,k_5}\Delta h_{\text{devol,2}} + \dot{\omega}_{\text{evap}}\Delta h_{\text{evap}} + \dot{\omega}_{\text{oxid}}\Omega_1\frac{\text{MW}_C}{\text{MW}_{O_2}}\Delta h_{\text{oxid}} + \dot{\omega}_{\text{steam,gasif}}\Omega_2\frac{\text{MW}_C}{\text{MW}_{H_2O}}\Delta h_{\text{steam,gasif}}$$

$$+ \dot{\omega}_{\text{CO}_2,\text{gasif}}\Omega_3\frac{\text{MW}_C}{\text{MW}_{\text{CO}_2}}\Delta h_{\text{CO}_2,\text{gasif}} + \dot{\omega}_{\text{CO,oxid}}\Delta h_{\text{CO,oxid}} + \dot{\omega}_{k_1}\left[\int_{T_0}^{T}(c_{P,\text{wood}} - c_{P,\text{non-cond. gases}})\,dT\right] + \dot{\omega}_{k_2}\left[\int_{T_0}^{T}(c_{P,\text{wood}} - c_{P,\text{tar}})\,dT\right]$$

$$+ \dot{\omega}_{k_3}\left[\int_{T_0}^{T}(c_{P,\text{wood}} - c_{P,\text{char}})\,dT\right] + \dot{\omega}_{\text{evap}}\left[\int_{T_0}^{T}(c_{P,\text{water}} - c_{P,\text{vapor}})\,dT\right] + (\dot{\omega}_{\text{steam,gasif}} + \dot{\omega}_{\text{oxid}} + \dot{\omega}_{\text{CO}_2,\text{gasif}})\left[\int_{T_0}^{T}(c_{P,\text{char}} - c_{P,\text{non-cond. gases}})\,dT\right]$$

$$+ \dot{\omega}_{k_4}\left[\int_{T_0}^{T}(c_{P,\text{tar}} - c_{P,\text{non-cond. gases}})\,dT\right] + \dot{\omega}_{k_5}\left[\int_{T_0}^{T}(c_{P,\text{tar}} - c_{P,\text{char}})\,dT\right]$$

$$(9)$$

Compared to earlier works by Haberle et al.,[19,21] minor corrections were made in the advective terms of the continuity equation, the species equations, and the energy equation. The initially used equations suggested by Lu et al.[4] were based on the phase-averaged gas density entering the convective term, while, based on physical consistency, the intrinsic gas density would be required. The corresponding typographical error in the advection term, with respect to intrinsic gas density and phase-averaged gas density, is also found in the review paper by Haberle et al.[1]

Furthermore, the diffusive terms in the species equations were corrected, compared to earlier works, since Kim et al.[22] suggested that the phase-averaged diffusive mass flux ($J_{\text{diff},k}$) should be calculated as

$$J_{\text{diff},k} = -D_{\text{eff}}\rho_g^g \nabla Y_k \tag{10}$$

if the effective diffusivity is calculated as

$$D_{\text{eff}} = \frac{\left(\frac{1}{\frac{1}{D_{\text{AB}}} + \frac{1}{D_{\text{Knudsen}}}}\right)\epsilon_g}{\tau} \tag{11}$$

as it is done in this work, where $\tau = \frac{1}{\epsilon_g}$. Of course, note that, depending on the definition of the effective diffusivity, either the intrinsic gas density enters the diffusive term or the phase-averaged gas density.

The density, temperature, and pressure of the gas phase are linked together by the equation of state. The gas-phase flow is modeled by Darcy's law.[4]

2.1. Boundary Conditions. The overall model setup is the same for the two different ash-handling concepts studied here, with the main difference being that, in Model A, the boundaries are fixed to the same grid point during the entire conversion, while the boundaries are moving inward with the char conversion front in Model B. The concept of inward moving boundaries is based on the idea that, as soon as char at a grid point has been consumed, the evolution equations at this grid point are assumed to not change anymore with time. The boundary conditions are then moved to the grid point further inward. Therefore, Model B requires tracking of the char conversion front. Hereby, the number of grid points is constantly reduced. When using Model A instead, evolution equations are continuously solved for the entire number of grid

Table 4. List of Species Source Terms and Gas-Phase Source Terms[a]

source term	equation	equation number
species k phase average density	$\rho_k = \rho_g^g \, \epsilon_g \, Y_k$	(12)
steam gasification[b]	$\dot{\omega}_{\text{steam,gasif}} = k_{H_2O}\rho_{H_2O,g}\tilde{s}_{a,\text{char}}$	(13)
char oxidation[b]	$\dot{\omega}_{\text{oxid}} = k_{O_2}\rho_{O_2}\tilde{s}_{a,\text{char}}$	(14)
CO_2 gasification[b]	$\dot{\omega}_{CO_2,\text{gasif}} = k_{CO}\rho_{CO_2}\tilde{s}_{a,\text{char}}$	(15)
CO oxidation	$\dot{\omega}_{CO} = k_{CO}\left(\dfrac{\epsilon_g\rho_g^g Y_{CO}}{MW_{CO}}\right)\left(\dfrac{\epsilon_g\rho_g^g Y_{O_2}}{MW_{O_2}}\right)^{0.25}\left(\dfrac{\epsilon_g\rho_g^g Y_{H_2O,g}}{MW_{H_2O}}\right)^{0.5}$	(16)
gas-phase source term	$\dot{\omega}_g = \dot{\omega}_{\text{oxid}}\dfrac{2MW_C}{MW_{O_2}} + \dot{\omega}_{\text{steam,gasif}}\dfrac{MW_C}{MW_{H_2O}} + \dot{\omega}_{CO_2,\text{gasif}}\dfrac{MW_C}{MW_{CO_2}} + (k_1 + k_2)\rho_{\text{wood}}$ $\qquad - k_5\rho_{\text{tar}} + k_{\text{evap}}\rho_b$	(17)
CO_2 source term	$\dot{\omega}_{CO_2} = f_{CO_2} k_1\rho_{\text{wood}} + g_{CO_2}k_4\rho_{\text{tar}} - \dot{\omega}_{CO_2,\text{gasif}} + \dot{\omega}_{CO}\dfrac{MW_{CO_2}}{MW_{CO}}$	
H_2O (g) source term	$\dot{\omega}_{H_2O,g} = k_{\text{evap,b}}\rho_b - \dot{\omega}_{\text{steam,gasif}} + f_{H_2O}k_1\rho_{\text{wood}} + g_{H_2O}k_4\rho_{\text{tar}}$	(18)
CO source term	$\dot{\omega}_{CO,\text{total}} = 2\dot{\omega}_{\text{oxid}}\dfrac{MW_{CO}}{MW_{O_2}} + f_{CO}k_1\rho_{\text{wood}} + g_{CO}k_4\rho_{\text{tar}} + \dot{\omega}_{\text{steam,gasif}}\dfrac{MW_{CO}}{MW_{H_2O}}$ $\qquad + 2\dot{\omega}_{CO_2,\text{gasif}}\dfrac{MW_{CO}}{MW_{CO_2}} - \dot{\omega}_{CO}$	(19)
H_2 source term	$\dot{\omega}_{H_2} = f_{H_2} k_1\rho_{\text{wood}} + g_{H_2}k_4\rho_{\text{tar}} + \dot{\omega}_{\text{steam,gasif}}\dfrac{MW_{H_2}}{MW_{H_2O}}$	(20)
tar source term	$\dot{\omega}_{\text{tar}} = k_2 \rho_{\text{wood}} - k_4 \rho_{\text{tar}} - k_5 \rho_{\text{tar}}$	
O_2 source term	$\dot{\omega}_{O_2} = -\dot{\omega}_{\text{oxid}} - \dot{\omega}_{CO}\dfrac{1MW_{O_2}}{2MW_{CO}}$	(21)
devolatilization reactions	$k_i = A_i \exp\left(\dfrac{-E_{a_i}}{RT}\right), \quad i = 1, 2, 3, 4, 5$	(22)
homogeneous reactions	$k_{CO} = A_{CO} \exp\left(\dfrac{-E_{a_{CO}}}{RT}\right)$	(23)
heterogeneous reactions	$k_k = A_k T \exp\left(\dfrac{-E_{a_k}}{RT}\right), \quad k = CO_2, O_2, \text{steam}$	(24)

[a]The fractions of gas species k produced from primary devolatilization reactions are marked by f_k, and the fraction of species k formed from secondary reactions is marked by g_k. [b]marks that the specific surface area used in this reaction term is corrected as follows: $\tilde{s}_{a,\text{char}} = s_{a,\text{char}}\left(\dfrac{\rho_{\text{char}}}{\rho_{\text{char}} + \rho_{\text{ash}} + \rho_{\text{wood}}}\right).$

points that have been assigned to the model at the beginning of the simulations. Therefore, boundary conditions are fixed. In Model A, shrinkage is then modeled such that the cell volume related to a grid point shrinks, because of drying and devolatilization. The new total volume of the wood particle is then calculated by summing up the different cell volumes, and the new grid spacing is calculated, based on the assumption of a structured equidistant grid, as well as a new wood particle radius.

The applied temperature boundary condition (for Models A and B) is[3]

$$\lambda_{\text{eff}} \frac{\partial T}{\partial r} = \sigma\omega_{\text{eff}}(T_{\text{wall}}^4 - T_{\text{surface}}^4) + h_c(T_g - T_{\text{surface}}) \tag{25}$$

where λ_{eff} is the effective thermal conductivity of the solid phase, T_{wall} the furnace wall temperature, ω_{eff} the effective particle emissivity, T_{surface} the particle surface temperature, T_g the surrounding gas phase temperature, and h_c the heat-transfer coefficient (reduced by the blowing factor). The current model does not consider the radiative feedback of the flame surrounding the particle. This is of course a simplification.

The boundary condition for the mass fractions of gas species k is defined as[3]

$$D_{\text{eff}} \frac{\partial Y_k}{\partial r} = h_m(Y_{k,\infty} - Y_{k,\text{surface}}) \tag{26}$$

where D_{eff} is the effective diffusivity, h_m the mass-transfer coefficient corrected by the blowing factor, $Y_{k,\infty}$ the mass

fraction of gas species k in the bulk, and $Y_{k,\text{surface}}$ the mass fraction of gas species k at the surface.

The reduction of heat- and mass-transfer coefficients by the blowing of the exiting gases (the Stefan flow) is considered by the following correlations:[23]

$$h_c = \frac{\dot{M}_{\text{total}}\overline{c}_{P,g}}{h_{c,0}\left[\exp\left(\dfrac{\dot{M}_{\text{total}}\overline{c}_{P,g}}{h_{c,0}}\right) - 1\right]} \tag{27}$$

for the heat transfer with $h_{c,0}$ being the uncorrected heat-transfer coefficient and $\overline{c}_{P,g}$ being the mass-averaged specific heat capacity of the gas mixture and

$$h_m = \frac{\dot{M}_{\text{total}}}{h_{m,0}\left[\exp\left(\dfrac{\dot{M}_{\text{total}}}{h_{m,0}}\right) - 1\right]} \tag{28}$$

for the mass-transfer coefficient, with $h_{m,0}$ being the uncorrected mass-transfer coefficient, and $\dot{M}_{\text{total}}$ being the total gas-phase mass flux leaving the particle. The Nusselt and Sherwood numbers (Nu and Sh, respectively) were calculated with the Ranz−Marshall correlation:[2]

$$Nu = 2 + 0.6Re^{0.5}Pr^{1/3} \tag{29}$$

and

$$Sh = 2 + 0.6Re^{0.5}Sc^{1/3} \tag{30}$$

where Re is the Reynolds number, Pr the Prandtl number, and Sc the Schmidt number.

Table 5. Properties Used as Input Values for the Drying, Devolatilization, and Char Conversion Model

property	units	value	ref(s)
thermal conductivity	W m^{-1} K^{-1}		
wood cell wall, $\lambda_{\text{wood},\perp}$		0.52	7
water, $\lambda_{\text{l},\perp}$		$0.278 + 1.11 \times 10^{-3}T$	7
ash, $\lambda_{\text{ash},\perp}$		1.2	4
char, $\lambda_{\text{char},\perp}$		0.071	10
gases, λ_{g}		25.77×10^{-3}	24
specific heat capacity	J kg^{-1} K^{-1}		
wood (298−413 K), $c_{\text{P,wood}}$		$-91.2 + 4.4T$	10
wood (350−500 K), $c_{\text{P,wood}}$		$1500 + T$	10
ash, $c_{\text{P, ash}}$		$754 + 0.586(T - 273)$	25
gases, $c_{\text{P, g}}$		$770 + 0.629T - 1.91 \times 10^{-4}T^2$	10
char, $c_{\text{P, char}}$		$420 + 2.09T - 6.85 \times 10^{-4}T^2$	10
tar, $c_{\text{P, tar}}$		$-100 + 4.4T - 1.57 \times 10^{-3}T^2$	10
vapor, $c_{\text{P,H}_2\text{O(g)}}$		$1670 + 0.64T$	10
apparent/true wood density^a	kg m^{-3}	570 and 1500 ($\rightarrow \epsilon_{\text{pore,0}} = 0.62$)	26
radiative thermal conductivity, λ_{rad}	W m^{-1} K^{-1}	$\dfrac{4\omega_{\text{eff}}\epsilon_{\text{pore}}d_{\text{pore}}T^3}{1 - \epsilon_{\text{pore}}}$	10
binary diffusivity, D_{AB}	m^2 s^{-1}	$3 \times 10^{-5}\left(\dfrac{T}{T_{\text{ref}}}\right)^{1.75}$	4 and 25
particle diameter, d_{P}	m	9.5×10^{-3} m	4
aspect ratio, AR		1	4
moisture content, M_{liquid}		40% (wet basis)	4
permeability			
$\kappa_{\text{wood} \perp}$		10^{-16} m^2	27
$\kappa_{\text{char} \perp}$		10^{-13} m^2	27
emissivity			
char, ω_{char}		0.95	4
wood, ω_{wood}		0.85	4
ash,^{b} ω_{ash}		0.85	
porosity			
ash, $\epsilon_{\text{pore,ash}}$		0.8	14
char, $\epsilon_{\text{pore,char}}$		0.8	14
shrinkage factor			
drying, θ_{m}		0.9	20
devolatilization, θ_{devol}		0.9	20

^{a}This value was calculated based on knowing the apparent density and the true density. ^{b}The same emissivity was assumed for wood and ash.

The Ranz−Marshall correlation was used, since the wood particle modeled was almost-spherical.

In Model B, the exterior of the char core is tracked and the governing equations are solved for the interior grid points, while the exterior grid points are assumed to not change over time. The definition of exterior and interior grid points in the explanation above is done such that the exterior grid points are the ones of the original mesh whose position is now outside of the boundary between the solid particle and the surrounding gas. Therefore, exterior grid points are grid points of the original mesh that are now located in the surrounding gas phase, since the solid species previously available have been fully consumed and now only the residual solid species ash could remain to be considered. Meanwhile, the internal grid points cover the points of the initial mesh that still span over solid species, i.e., the residual wood and char particle that has not yet been consumed.

The pressure at the particle surface is set to ambient pressure. The surrounding gas phase is assumed to be air. This is a simplification, because it neglects that different gas species can be the products of gas-phase reactions in the combustion chamber of, for example, a wood stove. The surrounding gas-

phase temperature was set to 1050 K, while the furnace wall temperature was set to 1276 K.

Furthermore, the model development is based on the following assumptions:

(1) All present phases are in local thermal equilibrium.
(2) An ideal gas is assumed.
(3) The superficial gas velocity can be calculated by using the Darcy velocity.
(4) Shrinkage is calculated from empirical shrinkage factors.
(5) The particle is surrounded by air.
(6) The effect of a surrounding flame is neglected.
(7) Wood properties change linearly from wood to char, as a function of the degree of conversion.

2.2. Numerical Setup. The wood properties entering the model are presented in Table 5.

The pore diameter, which is required for the calculation of the radiative contribution to the effective thermal conductivity, was based on pore diameters of 4×10^{-5} m for wood and 2×10^{-4} m for char.[10]

One advancement to other works was that, instead of using a constant diffusivity for all species, a temperature-dependent diffusivity is chosen, since it was assumed that the temperature

Table 6. Kinetic Data Used for Modeling Drying, Devolatilization, and Char Gasification and Oxidation[a]

reaction	reaction rate constant	units	ref	heat of reaction	ref
wood → gases	$k_1 = 1.11 \times 10^{11} \exp\left(\frac{-177\,000}{RT}\right)$	s^{-1}	28	−418 kJ kg^{-1}	29
wood → tar	$\downarrow k_2 = 9.28 \times 10^9 \exp\left(\frac{-149\,000}{RT}\right)$	s^{-1}	28	−418 kJ kg^{-1}	29
wood → char	$k_3 = 3.05 \times 10^7 \exp\left(\frac{-125\,000}{RT}\right)$	s^{-1}	28	−418 kJ kg^{-1}	29
tar → gases	$k_4 = 4.28 \times 10^6 \exp\left(\frac{-107\,500}{RT}\right)$	s^{-1}	30	42 kJ kg^{-1}	31
tar → char	$k_5 = 1 \times 10^5 \exp\left(\frac{-107\,500}{RT}\right)$	s^{-1}	32	42 kJ kg^{-1}	31
$\rho_b \to \epsilon_g \rho_g^g Y_{vap}$	$k_{evap} = 5.13 \times 10^{10} \exp\left(\frac{-88\,000}{RT}\right)$	s^{-1}	33	−2440 kJ kg^{-1}	4
C + xO$_2$ → aCO + bCO$_2$	$k_{oxid} = 1.715T \exp\left(\frac{-74\,800}{RT}\right)$	m s^{-1}	7	110 kJ mol^{-1} (fraction a)	b
				393.5 kJ mol^{-1} (fraction b)	b
C + H$_2$O → CO + H$_2$	$k_{H_2O,gasif} = 3.42T \exp\left(\frac{-130\,000}{RT}\right)$	m s^{-1}	4	−10 940 kJ kg^{-1}	b
C + CO$_2$ → 2CO	$k_{CO_2,gasif} = 3.42T \exp\left(\frac{-130\,000}{RT}\right)$	m s^{-1}	4	−14370 kJ kg^{-1}	b
CO + 0.5O$_2$ → CO$_2$	$k_{CO,oxid} = 10^{12.35} \exp\left(\frac{-167\,000}{RT}\right)$	s^{-1}	20	10 110 kJ kg^{-1}	4

[a]The term "Gases" in this table refers to noncondensable gases. [b]The heat of reactions have been calculated by assuming char reacting as pure carbon.
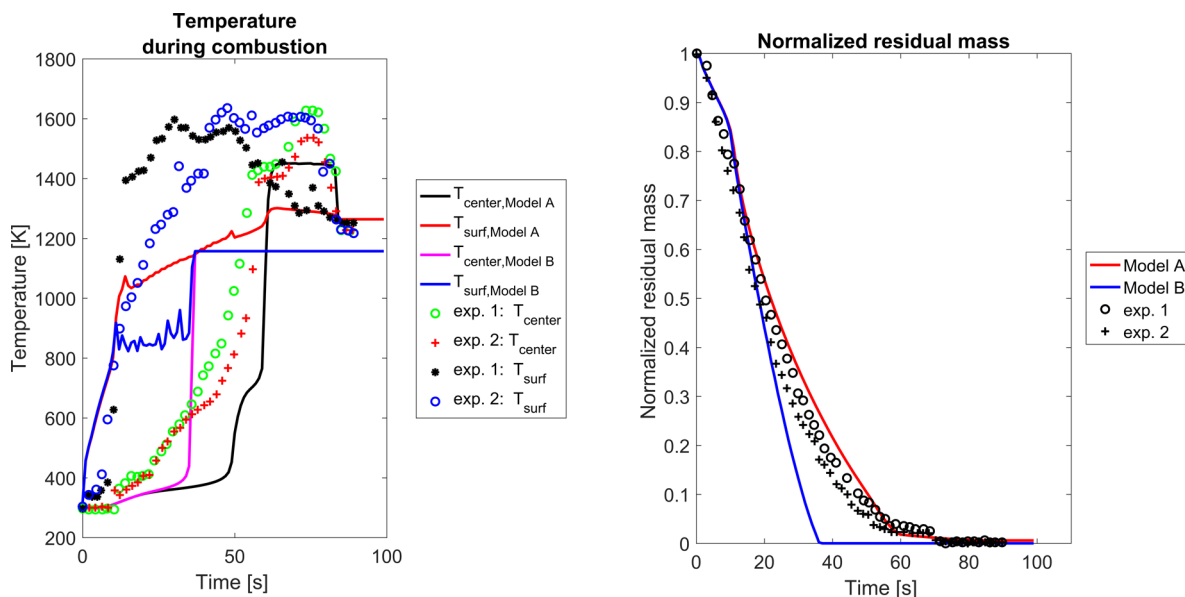

Figure 1. Temperature and normalized residual mass predicted by Models A and B with the surrounding gas-phase velocity being u_g = 0.5 m s^{-1}. The surface temperature is represented by T_{surf}; the center temperature is represented by T_{center}. The symbols are experimental data obtained by Lu et al.:[4] The measured T_{surf} are plotted by open blue circles (O) and black asterisks (*). The measured T_{center} are plotted as open green circles (O) and red crosses (+). The measured data for the normalized residual mass has been plotted as open black circles (O) and black crosses (+).

significantly influences the diffusion coefficient. Furthermore, a general D_{AB} was chosen. With respect to all the gaseous species formed from devolatilization, only H$_2$ has a significantly higher diffusivity, compared to the residual species. Hydrogen formation from primary and secondary devolatilization is comparably small, compared to carbon monoxide and carbon dioxide, as well as tar. Therefore, we assumed that a general D_{AB} value was a valid simplifying assumption.

The wood conductivities listed in Table 5 are for wood fiber and are therefore higher than what is commonly observed for effective wood thermal conductivities.

The applied pre-exponential factors, activation energies, and heat of reactions used for drying, devolatilization and char conversion are listed in Table 6.

Char oxidation is modeled by the following coefficients,[34] where a refers to the number of moles of carbon monoxide and b refers to the number of moles of carbon dioxide,

$$a + b = 1 \tag{31}$$

and where x refers to the number of moles of oxygen,

$$x = \frac{a}{2} + b \tag{32}$$

The ratio between CO/CO$_2$ was modeled to be temperature-dependent, according to[34]

$$\frac{a}{b} = A \exp\left(-\frac{E_\eta}{T}\right) \tag{33}$$

The coefficients A and E_η were taken to be 12 and 3300 K, respectively.[35]

Hydrogen oxidation reaction is not considered, because of limited hydrogen production during thermochemical conversion.

2.3. Numerical Solver and Discretization Schemes. The IDA solver, included in the SUNDIALS software package, is used to solve the set of differential and algebraic equations.[36] The convective term is discretized by first-order upwinding, while the diffusive terms are discretized by second-order central difference. Therefore, the accuracy in space is first-order, while the accuracy over time is dependent on the order of the backward differentiation formula, which can range from 1 to 5. The maximum time step was 10^{-4} s. The simulations were performed with 55 grid points spanning over the particle radius, as this number of grid points has been found to yield grid-independent solutions.

3. RESULTS AND DISCUSSION

In this section, the results of the parametric study, as well as the results of the comparison between the modeling results
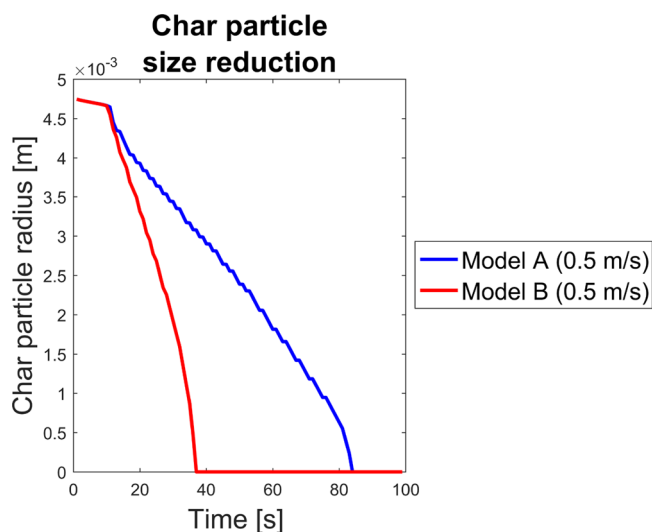
Figure 2. Comparison of char particle size (neglecting ash layer) reduction obtained by Models A and B.

obtained from the two different ash modeling concepts, are presented. The two different ash modeling concepts, based on fixed boundaries and inward-moving boundary conditions, are referred to as Models A and B, respectively, in this work.

3.1. Comparison of Models A and B. All simulations presented in this section were performed with a specific surface area of 10^6 m^2 m^{-3}. The temperature and the normalized residual mass predictions of the two modeling approaches are compared. Only these data are compared in this study, since they are thought to be the most representative ones. Therefore, based on these data, the applicability and suitability of a modeling approach can be sufficiently discussed.

From an experimental point of view, Figure 1 clearly shows that there is a significant difference between the different experimental test runs, especially when it comes to the measured surface temperatures. However, this derivation from measured surface temperatures is assumed to result from the difficulty involved in exactly measuring the surface temperature of a particle that is subject to significant size reduction due to

char consumption. Therefore, it can be assumed that a surface thermocouple might be detached at some point during the measurements, which led to the differences in measured data, causing the deviation visible with respect to the two experimental series. Further details on the experiments can be found in the original paper by Lu et al.,[4] who conducted the experiments.

Figure 1 shows that the two modeling concepts yield different total thermal conversion times, as well as center and surface temperatures. We also found that, for Models A and B, a lower surrounding gas-phase velocity (the test case was $u_{gas} = 0.25$ m s^{-1}) resulted in negligible influence on the total conversion time.

When the ash layer is removed immediately after char consumption has been accomplished (Model B), the conversion is faster than in Model A. This is because Model B does not consider any limitation to mass transfer of oxygen to the active sites through the ash surrounding the char core. Oxygen that has been transferred from the bulk to the char surface can directly react at the char surface. The additional consideration of diffusion through the porous ash layer, as it is done by Model A, reduces the amount of available oxygen at the surface of the residual char core and hereby also the burnout rate, while increasing the burnout time. The differences in initial normalized residual mass predictions obtained by Models A and B are initially minor, but become more prominent after 14 s. The reason for this is that the char at the outermost grid point has then been consumed, and, because of the different handling of the boundaries, the models start to predict very different conversion trends from this time forward.

Also, the temperature predictions are very different. Model B predicts a temperature plateau for T_{surf} at ∼850−950 K. At this temperature, enhanced char conversion reactions occur. Since Model B assumes that the boundary moves one grid point inward, after the char at a certain grid point has dropped below a threshold value, also the plotted surface temperature moves one grid point inward. This explains why the plotted surface temperature fluctuates within a range of enhanced char conversion temperatures at ∼850 K.

Most interesting is also to see that the final surface and center temperatures predicted by Model B remain at a lower level than the temperatures predicted by Model A. This observation is because Model B is based on the assumption of inward moving boundary conditions. As soon as the char mass at a grid point has been consumed, the boundary is shifted further inward, and hereby moves closer to the wood particle center. However, the grid point that had previously been consumed is then neglected in further evolution considerations, because it is assumed to not change over time anymore. This implies that the grid point is not allowed to further heat up after the complete char conversion. Therefore, the temperature at a grid point will remain at temperatures lower than the furnace wall temperature, if the grid point has not reached the furnace wall temperature before or during complete char conversion.

It is assumed that the temperature starts to increase above the previous temperature plateau between 850 K and 950 K, when the char at the last two innermost grid points is consumed. The two grid points degrade simultaneously and the heat release is higher on a particle level. Therefore, the temperature increases again before reaching the temperature plateau at 37 s.
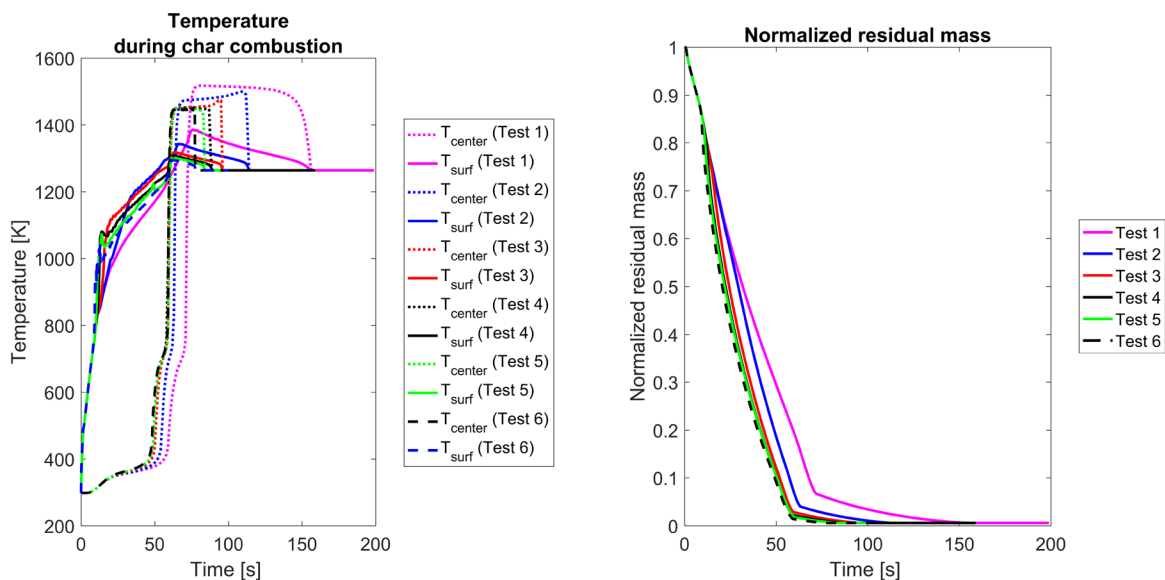
(a) Comparison of modeling results for center and surface temperature.

(b) Comparison of normalized residual mass.

Figure 3. Temperature and normalized residual mass predictions obtained from Tests 1−6 ($s_{a,char} = 10^2 - 10^7$ m^2 m^{-3}). The surface temperature is referred to as T_{surf} and the center temperature is referred to as T_{center}.
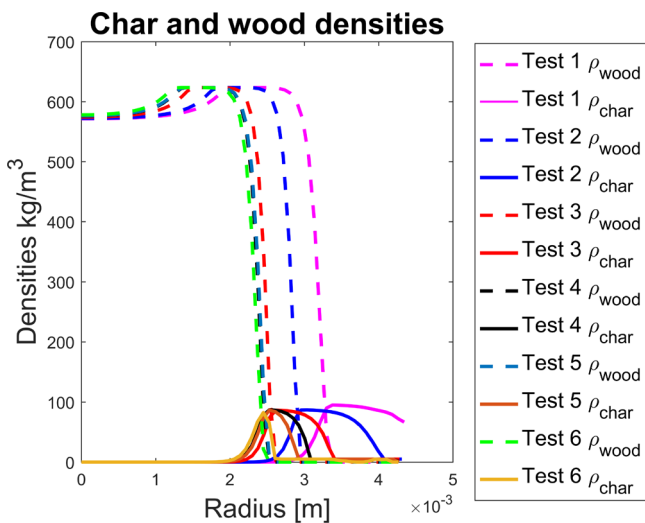

Figure 4. Comparison of predicted wood and char densities predicted with Tests 1−6 at 25 s.

Table 7. Tested Thermal Conductivities for Wood and Char[a]

| test case	$\lambda_{wood,\perp}$ (W m^{-1} K^{-1})	ref	$\lambda_{char,\perp}$ (W m^{-1} K^{-1})	ref
Test A	0.52	7	0.071[b]	10
Test B	0.43	37	0.071[b]	10
Test C	$0.291 + 0.000276T$	38	0.071[b]	10
Test D	$0.13 + 0.0003(T - 273)$[b]	39	0.071[b]	10
Test E	0.52	7	$0.091 + 8.2 \times 10^{-5}T$[b]	40
Test F	0.52	7	$1.47 + 1.11 \times 10^{-3}T$	3

[a]Each combination of thermal conductivity of char and wood is labeled as listed in the first column, e.g., Test A, which is subsequently used for discussion in the text section. [b]These thermal conductivities are effective solid species thermal conductivities.

However, it shall be outlined that the flat temperature line in Figure 1, with respect to Model B, does not have an actual physical meaning, since, according to the modeling assumption, there is no solid species left, whose temperature could be measured by thermocouples attached to the particle surface. In fact, the physical meaning of the blue and pink lines in Figure 1a stops at 37 s, which is at the instant when the temperature plateau becomes prominent.

The char consumption of the final char core occurs faster in Model B than in Model A, since oxygen transfer to the char core is more enhanced, because of the missing ash layer. The effective residual particle size is even more reduced, compared to what is predicted by Model A. A reduced residual particle diameter results in an enhanced mass-transfer rate to the residual char core. Consequently, Models A and B are also predicting different mass- and heat-transfer coefficients, since different effective particle diameters are used for their calculations.

One can see the different char conversion behaviors, when plotting the change in char particle radius over time (Figure 2). The initial, rather slow, decrease in particle size is due to volumetric shrinkage during drying and devolatilization, which is then superimposed by the more prominent size reduction of the outer particle areas where char conversion occurs.

Overall, it was found that temperature and normalized residual mass predictions obtained with Model A are in better agreement with experimental data. Although we found that the two modeling concepts yield different results, the conclusion is drawn that, based on these results, we cannot generically state which model is more appropriate. In fact, it is not yet known if the better agreement with experiments observed for Model A is due to the applied fuel (and its ash content, as well as the chemistry of the ash) or due to the idealized experimental conditions in the single particle reactor. This conclusion is based on the understanding that the validation experiments are performed under idealized conditions in a single particle reactor (i.e., no influence of other particles). Under such
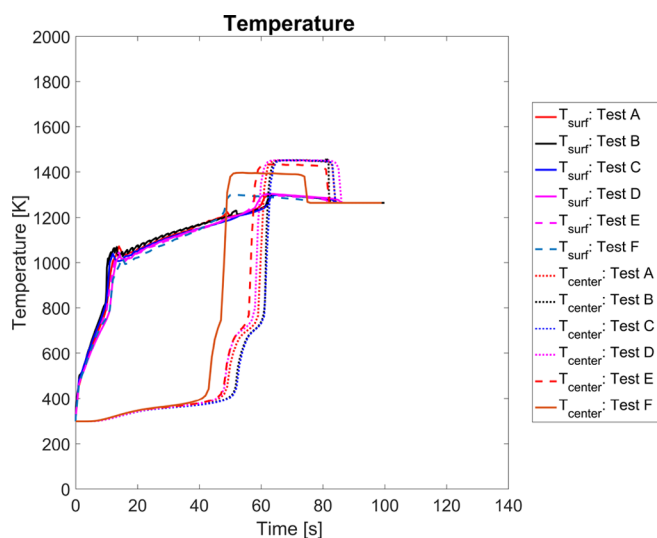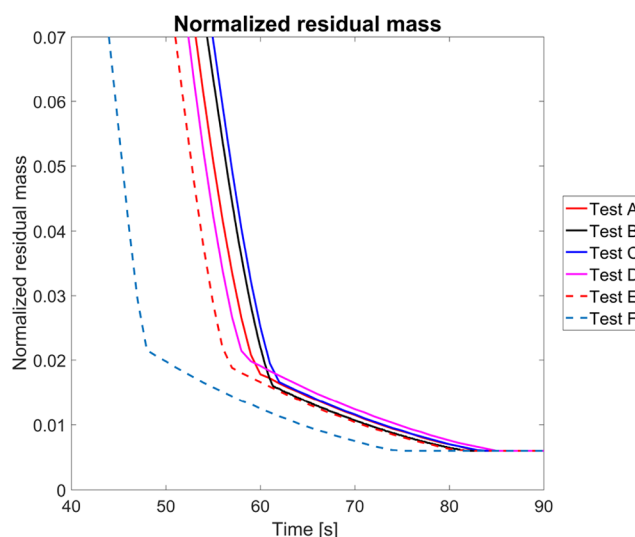
(a) Center and surface temperature.
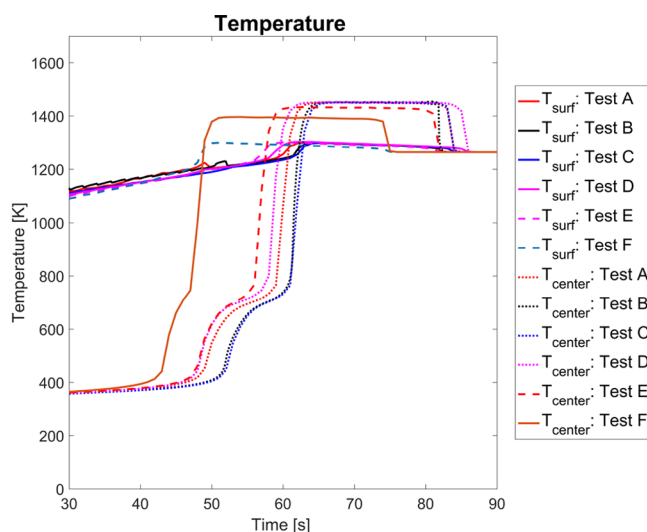
(b) Zoom of left hand panel.
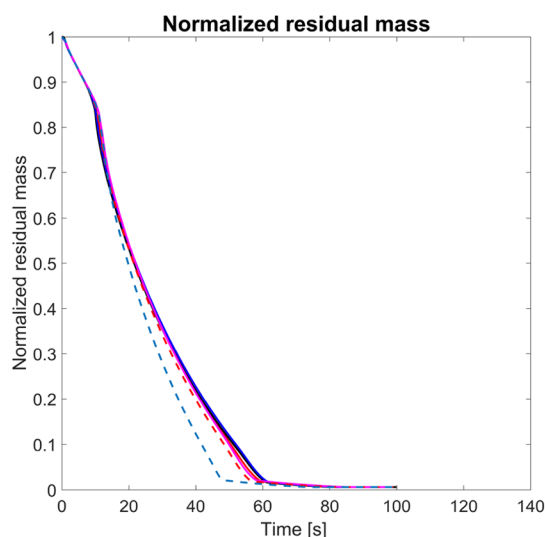
(c) Normalized residual mass.

(d) Zoom of left hand panel.

Figure 5. Temperature and normalized residual mass predictions obtained from Tests A−G. All tests are done with $s_{a,char} = 10^6$ m^2 m^{-3} and u_{gas} = 0.5 m s^{-1}. The surface temperature is referred as T_{surf}, and the center temperature is referred as T_{center}.

conditions, the up-build of an ash layer is not affected by external phenomena. However, in a wood stove, wood logs are stacked. Therefore, fragmentation of upper wood logs might affect the physical appearance of lower wood logs by off-falling parts and the subsequent knockoff of the brittle and fragile ash of the lower wood logs. This implies that, under conditions found in wood stoves, it is more likely that the ash layer will not be built up undisturbedly, but, instead, will fall off.

This phenomenon is of course a local structural change of the particle. Therefore, Models B and A are two extreme cases that simplify a structural change by assuming that the entire surface of the particle can be handled equally (e.g., homogeneous boundary conditions). However, to consider a localized knockoff of char, or a localized change in the ash appearance due to fusion, which could locally affect heat and mass transfer, multidimensional models are needed.

Therefore, in order to validate which modeling concept is more appropriate for solid phase conversion modeling in wood stove applications, the concept can not only be linked to the ash content and composition of the fuel, but also must be chosen in dependence of the operating (experimental) conditions. Therefore, further studies and model developments are recommended to eventually be able to obtain an accurate replication of this structural change in numerical models.

3.2. Parametric Study. To assess the sensitivity of the model to specific surface areas and the thermal conductivities of char and wood, as well as gas permeabilities, a parametric study over these parameters was performed. For all of these input parameters, there is a wide range of values available in the literature. This scattering of available data can affect modeling results, and, therefore, it is needed to study to which extent the results are influenced. The parametric study was
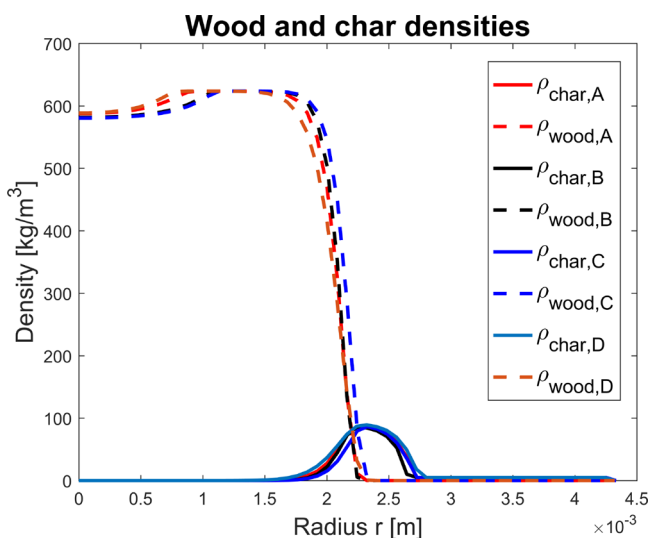
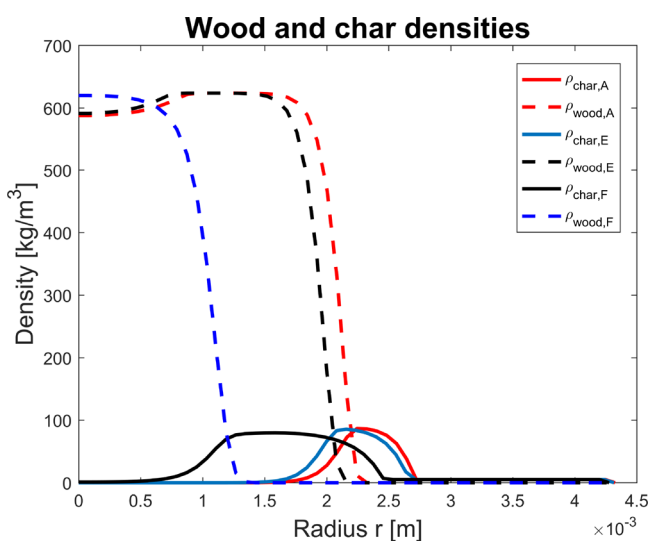**Figure 6.** Comparison of devolatilization zones predicted with Tests A−D at 45 s.

Figure 7. Comparison of devolatilization zones predicted with Tests A, E, and F at 45 s.

done with Model A (fixed boundaries) and a surrounding gas-phase velocity of 0.5 m s^{-1}.

3.2.1. Specific Surface Area. When studying the sensitivity of the model to the specific surface area of char, a range of values were tested. The maximum value tested was $s_{a,char,max} = 10^7$ m^2 m^{-3} (Test 6), and the second largest value was $s_{a,char} = 10^6$ m^2 m^{-3} (Test 5), which was the standard value that we used in all of the other simulations presented in this paper. The minimum value that was tested was $s_{a,char,min} = 10^2$ m^2 m^{-3} (Test 1). Furthermore, the intermediate values of $s_{a,char} = 10^3$ m^2 m^{-3} (Test 2), $s_{a,char} = 10^4$ m^2 m^{-3} (Test 3), and $s_{a,char} = 10^5$ m^2 m^{-3} (Test 4) were tested. The values were chosen such that they covered a broad range of values, replicating the significant scattering of data found in the literature (see Table 2).

It was found that if the specific surface area is smaller than a critical value then the reactivity of the char has an influence on modeling results, especially on the final char conversion stage (see Figure 3). A very low reactivity (implemented in model considerations by a low specific surface area, i.e., Test 1) yielded a significantly slower char conversion. The overall

conversion times were 156 s for Test 1, 113 s for Test 2, 96 s for Test 3, 88 s for Test 4, 84 s for Test 5, and 77.5 s for Test 6. The differences between Test 5 and Test 6 are small. Test 1 led to significantly slower char conversion. In fact, when it comes to the pure char conversion time, the results are as theoretically expected: predicting that a significantly low specific surface area results in longer char conversion, because of reduced char oxidation and gasification rates. Still, it is interesting to see that, even though Test 1 (and also Test 2, to a certain extent) differs significantly from the other test runs, the four residual test runs predict a more similar behavior. In fact, the predicted results of the higher specific surface area test runs converge, which implies that the specific surface area does not have a significant influence on the model results anymore if mass transfer starts to control oxidation. This means that, if the specific surface area is above a certain critical threshold, the char conversion rate becomes independent of the choice of specific surface area. The reason is that as long as the reactivity is set to be significantly large (large enough surface area), the oxygen diffusion to the active sites is the limiting factor and not the chemistry of char conversion.

In Figure 4, one can identify the char conversion layer (thickness and position), as well as the devolatilization zone, plotted at 25 s. The apparent dry wood density increases even above the initial value, which is due to ongoing volumetric shrinkage, which is considered to occur during drying and devolatilization in this model. At this early stage of conversion, one can still identify the ordering of the char conversion front, according to the specific surface area. This means that, for the highest specific surface area, the char conversion front has moved furthest inside. The reason for this ordering is due to the start of char conversion at the outermost grid point. The rate of this grid point's conversion is not limited by the availability of oxygen, but is controlled by specific surface area. This implies that a higher specific surface area allows this grid point to react faster. Overall, char conversion therefore starts at a slightly earlier time.

As the char conversion front moves inward, the char conversion is diffusion-controlled, such that the advancement of the test case with the highest specific surface area is constantly reduced, since, for all high-specific-surface-area test cases (Tests 4−6), oxygen diffusion is controlling. Since 25 s, however, is still an early time in the total conversion, we still see the advancement of the highest-specific-surface-area test case rather prominently.

Since the heat release due to char conversion then also occurs to a close-to-same extent, independent of the choice of specific surface area, and the thermal properties of the char ash layer surrounding the dry wood are similar (which is due to the similar degree of conversion), also the heat-transfer-controlled phenomena occurring further inside the particle, such as devolatilization, have a tendency to converge for the high-surface-area test cases (Tests 4−6) (see Figure 4).

From the right-hand panel of Figure 3, one can see that the kink in normalized residual mass predictions, indicating where devolatilization has been accomplished in the entire particle, and where only char conversion is occurring on a particle scale, varies, depending on the specific surface area. It is highest for the lowest specific surface area, which implies that more char is still available, contributing more to the normalized residual mass, while for higher specific surface areas, the kink occurs at lower residual mass. This suggest that more char has already been consumed in the outer particle area, while devolatilization
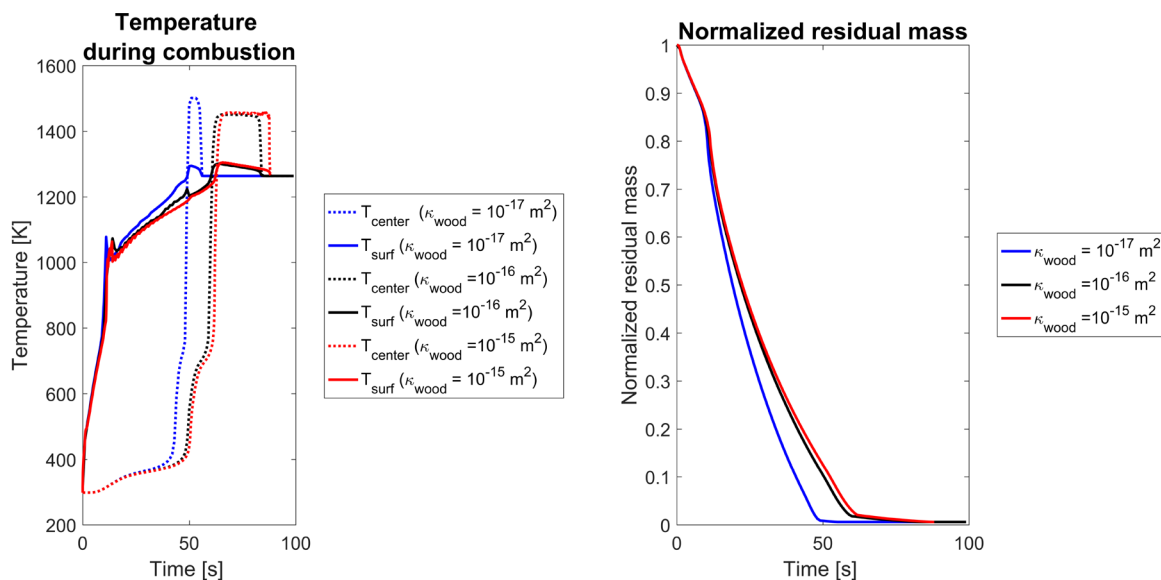
(a) Surface and center temperature predictions obtained from *Test 1*, *Test 2* and *Test 3*.

(b) Normalized residual mass predictions obtained from *Test 1*, *Test 2* and *Test 3*.

Figure 8. Sensitivity of modeling results to assigned wood and char permeabilities. Test 1 was run with $\kappa_{wood} = 10^{-17}$ m^2 and $\kappa_{char} = 10^{-14}$ m^2; Test 2 was run with $\kappa_{wood} = 10^{-16}$ m^2 and $\kappa_{char} = 10^{-13}$ m^2; Test 3 was run with $\kappa_{wood} = 10^{-15}$ m^2 and $\kappa_{char} = 10^{-12}$ m^2.

is still proceeding in the inner particle areas. These observations outline that, in thermally thick particles, all three conversion stages are strictly coupled and cannot be examined separately in modeling works.

The differences between Test 6 and Test 5 are small. In fact, when looking at the final enhanced char conversion time, which is defined as the time when only a char particle is left, the variation in the contribution of this final conversion stage to the total conversion stage, varies from 29% to ~24%, respectively, for Test 5 and Test 6. This final conversion time can be identified in Figure 3b as the time after the kink in the normalized residual mass prediction. Compared to Test 1, where this final char conversion time is 54% of the total conversion time, the difference between Test 5 and Test 6 can be considered negligible.

From this study on the influence of specific surface areas, it is concluded that, as soon as a critical value of specific surface area is exceeded, while, at the same time, modeling oxygen diffusion to the char core through the ash layer, the char conversion is not affected by the char specific surface area. Accordingly, one might assume that, unless a comparably low char surface area is chosen, the influence of char reactivity on modeling results is minor.

However, it needs to be outlined that this critical specific surface area is no generic value but, in fact, is case-dependent, as it will be influenced by experimental conditions, i.e., external temperature and heating rate, and fuel properties.

3.2.2. Thermal Conductivity. Since both drying and devolatilization are heat-transfer-controlled phenomena, it was aimed to investigate how the thermal conductivities affect the modeling results. Only the influence of the thermal conductivities of wood and char were studied, since both will have a significant influence on the heat conduction. The results will be less sensitive to the thermal conductivity of the gas, since the fraction of the heat that is conducted by the gas is significantly smaller than it is for the solid species.

Furthermore, the model's sensitivity to the thermal conductivity of ash was not studied. The variation in applied thermal conductivities of ash found in other works was considered minor.

All simulations presented in this section were performed with a specific surface area of 10^6 m^2 m^{-3} and a surrounding gas-phase velocity of 0.5 m s^{-1}. The different conductivities that were tested are listed in Table 7.

The validity of the temperature dependence of thermal conductivity of wood, calculated as suggested in Test C, is limited to a maximum temperature of 500 °C.[41] For wood devolatilization modeling, the thermal conductivity as defined in Test C can be used, since most of the wood will have been consumed at temperatures of >500 °C.

In the original papers, where the thermal conductivities were obtained, the thermal conductivity of char used in Test F is assuming the thermal conductivity of the char without pores, requiring the multiplication by char porosity, according to

$$\lambda_{char,eff} = (1 - \epsilon_{char})\lambda_{char,fiber} \tag{34}$$

in order to model the effective thermal conductivity of char.

It was found that the thermal conductivity of Test F led to significantly higher thermal conductivities than the temperature dependencies of Test E.

The thermal conductivities of wood and char affect the internal temperature history (as shown in Figure 5). Drying and devolatilization stages are accomplished earliest for Test F and are terminated the latest by Tests B and C. The difference between Test B and Test C is minor, since, even though the effective wood thermal conductivity of Test C is lower at room temperature, it increases as the temperature increases while Test B considers a constant value. Since the two modeling test runs are so similar, it is somewhat expected that the difference in thermal conductivities at room temperature is balanced during the conversion as the temperature dependence becomes more important. In fact, Test F leads to a comparably fast

internal heating of the particle, since it has the least insulating char layer of all test cases. Therefore, the heat transferred to the external particle surface can easily be conducted further inside, even though a char layer is built up.

It can be observed that the drying stage is influenced by the choice of thermal conductivity of wood. This can be seen by Tests B and C, which have a lower thermal conductivity of wood (at room temperature), compared to Test A, and therefore predict a slower drying. When both drying and devolatilization are studied, the influence of thermal conductivity of char becomes relevant. The more insulating the char layer is, the more the progress of the devolatilization zone slows.

When looking at Figure 5, one can observe that, for Tests B and C, the drying and the devolatilization stage are accomplished the latest, compared to other test cases. Drying is considered to have been accomplished in the entire particle when the center temperature starts to exceed 400 K. Devolatilization is assumed to have been accomplished in the entire particle when the final kink in the normalized residual mass prediction can be seen.

By the choice of thermal conductivity, the internal heat transfer is changed, which can result in accelerated or retarded drying and devolatilization of the inner areas of a thermally thick wood particle. The thermal conductivity of wood does not only significantly affect drying but also the predevolatilization temperature heating of the particle. This has an effect on the char conversion stage, whose start is accelerated or retarded accordingly.

If internal heat transfer is retarded, the heating of the particle to temperatures where char consumption reactions occur is slower, which then again is reflected by a longer total conversion time of the particle.

In Figure 6, the char and wood densities at 45 s are plotted to outline how the thermal conductivity of wood affects the devolatilization zone. It is seen that the position of the devolatilization zone is affected by the assigned thermal conductivity of wood, even though the predicted shift in the devolatilization zone is minor, with respect to the tested range of thermal wood conductivities. The devolatilization zone has moved furthest inside for Test D, which has the highest thermal conductivity of wood at high temperatures. A higher thermal conductivity of wood leads to a faster heating of the inner particle areas in predevolatilization temperature ranges and, therefore, fast termination of drying.

After studying the effect of thermal conductivity of wood, the influence of the thermal conductivity of char on the temperature history and residual mass was studied. Modeling of temperature evolution and mass loss trends were performed with char thermal conductivities as used in Tests A, E, and F.

Figure 7 shows that the devolatilization zone moves faster when using a higher thermal conductivity of char. This observation agrees with the theoretical understanding that the lower the insulating barrier is, the faster the heat-transfer-controlled phenomena are. Again, the sensitivity of the modeling results to thermal conductivities seems significant, which can be seen by the significant shift in devolatilization zones predicted by Tests A and F.

3.3. Gas Permeability. When studying the influence of gas permeability on modeling results, three cases were tested. In Test 2, the gas permeability for wood was fixed to 10^{-16} m^2 and the one for char was set to 10^{-13} m^2. In the second test (Test 1), the wood permeability was set to 10^{-17} m^2 and the

char permeability was set to 10^{-14} m^2; and, in Test 3, κ_{wood} was fixed to 10^{-15} m^2 and κ_{char} was fixed to 10^{-12} m^2. The difference between wood and char permeabilities in all test cases was a factor of 1000. The specific surface area for the test runs was set to 10^6 m^2 m^{-3} and the surrounding gas-phase velocity was set to 0.5 m s^{-1}. The modeling concept presented in Model A was used for the study.

A parametric study on the gas permeability was performed in order to study its effect on the particle temperature history, as well as the normalized residual mass predictions. When testing a range of different permeabilities, it was observed that higher permeabilities have an effect on the stability of the numerical solution procedure.

It can be seen from Figure 8 that the permeabilities influence both the temperature and the normalized residual mass predictions. When higher permeabilities are used, the termination of drying and devolatilization is shifted to slightly later times, which therefore also shifts the start of the final char conversion to later times.

The difference between Test 2 and Test 3 is only minor, compared to the difference between predictions obtained by Test 2 and Test 3 and predictions obtained by Test 1. This effect of permeability on devolatilization is due to its influence on the diffusive mass transfer within the particle. The relevant point here is that lower permeabilities yield lower superficial velocity. A lower outward superficial velocity allows for more diffusive mass transfer into the particle. The consequence of this is that the ratio of diffusive transport of oxygen into the particle, relative to the outwardly convective transport of oxygen due to the gaseous flow within the particle, becomes larger, because of the lower convective velocity. Therefore, char conversion is faster, which results in additional heating of the particle, because of exothermic char oxidation, which additionally accelerates the drying and devolatilization.

The total conversion time only increased from 84 s to 87.5 s for Test 2 and Test 3, respectively, while it was only 55 s in Test 1. The final char conversion time ranged from 28.6% to 29.3% of the total conversion time for Tests 2 and 3, respectively, while it covered only 11% of the total conversion time in Test 1. Based on these results, one can conclude that, for a permeability above a certain value, the total conversion time, as well as predicted center and surface temperatures, become independent of permeability. However, wood internal pressure distributions will still be affected by the permeabilities, but the variations are of minor influence to general solid-phase degradation behavior, e.g., solid mass loss trends. In the opposite case, when the permeability is below the critical value, the influence of gas permeability on the result is significant.

4. CONCLUSIONS

In this work, two different modeling approaches for ash handling in wood combustion modeling were tested. In one approach, an ash layer builds up around the unreacted char core and, therefore, must be considered in heat and mass transfer. In the second modeling approach, the ash remaining after total char conversion at a given point falls off immediately, such that no ash layer builds up around the char core. Hereby, the model operates in the absence of an ash layer and, therefore, a lack of influence of the ash layer on heat and mass transfer. It was found that the two modeling approaches give very different results, with the modeling approach of no ash-layer buildup yielding faster conversion. However, the modeling approach with the distinct consid-

eration of an up-building ash layer gave temperature and normalized residual mass predictions that were in better agreement with experimental observations. Nonetheless, it was concluded that the better agreement can also be due to the idealized experimental conditions tested in the single particle reactor, and therefore the unhindered up-building of an ash layer.

Therefore, it is expected that, for real wood stove conditions, the approach where the ash layer falls off may still be more realistic, since the occurrence of knocking off of ash is more realistic under those conditions. However, it must be added that, in the current numerical setup, even the consideration of such a knockoff is simplified, since it is assumed to occur continuously as degradation proceeds and homogeneously at the lateral surface of the wood particle. The knockoff, as in wood stoves, however, would be a local phenomenon. Therefore, Models A and B, as presented in this work, are two extreme cases. The actual case given in a wood stove will be a mixture of the two extreme cases. To capture such a mixed case, however, which requires the localization of the knock-off phenomenon, is expected to require multidimensional models, where the external surface of the wood log is well enough considered. Therefore, future work is recommended to focus on multidimensional wood log models.

Furthermore, we also present a parametric study of thermal conductivities of wood and char, the specific surface area, and the gas permeabilities. It was found that the model is very sensitive to the thermal conductivity of wood and char; this observation is because drying and devolatilization are both heat-transfer-controlled phenomena.

The model is also sensitive to the specific surface area if it is less than a critical value. If the char surface area is large, such that diffusion controls char conversion, the assumed specific surface area is a less critical input data.

When testing the model's sensitivity to gas permeability, it was found that total wood combustion was dependent significantly on assigned permeabilities until a critical value was reached.

■ AUTHOR INFORMATION

Corresponding Authors
*E-mail: inge.haberle@ntnu.no (I. Haberle).
*E-mail: nils.e.haugen@sintef.no (N. E. L. Haugen).
ORCID ⓘ
Inge Haberle: 0000-0002-3945-3627
Notes
The authors declare no competing financial interest.

■ ACKNOWLEDGMENTS

■ NOMENCLATURE

A = pre-exponential factor $[s^{-1} \ (m \ s^{-1} \ K^{-1})^{-1}]$
AR = aspect ratio
c_P = specific heat capacity $[J \ kg^{-1} \ K^{-1}]$
D_{AB} = diffusivity $[m^2 \ s^{-1}]$
D_b = bound water diffusivity $[m^2 \ s^{-1}]$
D_{eff} = effective diffusivity $[m^2 \ s^{-1}]$
$D_{Knudsen}$ = Knudsen diffusion $[m^2 \ s^{-1}]$

d_P = particle diameter $[m]$
d_{pore} = pore diameter $[m]$
E_a = activation energy $[J \ mol^{-1}]$
f = gas species fraction from primary devolatilization
g = gas species fraction from secondary devolatilization
Δh = heat of reaction $[J \ kg^{-1}]$
$h_{c,0}$ = heat-transfer coefficient without Stefan flow $[W \ m^{-2} \ K^{-1}]$
h_c = heat-transfer coefficient with Stefan flow $[W \ m^{-2} \ K^{-1}]$
$h_{m,0}$ = mass-transfer coefficient without Stefan flow $[m \ s^{-1}]$
h_m = mass-transfer coefficient with Stefan flow $[m \ s^{-1}]$
J_{diff} = diffusive mass flux $[kg \ s^{-1} \ m^{-2}]$
k = reaction rate constant $[s^{-1} \ or \ m \ s^{-1}]$
k_1 = reaction: wood to noncondensable gases
k_2 = reaction: wood to tar
k_3 = reaction: wood to char
k_4 = reaction: tar to noncondensable gases
k_5 = reaction: tar to char
M_{liquid} = liquid moisture content
$\dot{M}_{total}$ = total mass flux of exiting gases $[kg \ s^{-1} \ m^{-2}]$
MW = molecular weight $[kg \ mol^{-1}]$
R = ideal gas constant $[J \ mol^{-1} \ K^{-1}]$
r = radius $[m]$
T = temperature $[K]$
T_{gas} = surrounding gas-phase temperature $[K]$
T_{pyro} = pyrolysis temperature $[K]$
T_{ref} = reference temperature $[K]$ (298 K)
T_{wall} = furnace-wall temperature $[K]$
$s_{a,char}$ = specific surface area of char $[m^2 \ m^{-3}]$
u_b = bound-water velocity in the radial direction $[m \ s^{-1}]$
u_r = gas-phase velocity in the radial direction $[m \ s^{-1}]$
V_j = cell volume $[m^3]$
Y = mass fraction

Greek Letters

ϵ_g = gas-phase volume fraction
ϵ_{pore} = porosity
ω_{eff} = effective emissivity
Ω = stoichiometric coefficient
Φ = heat source term $[J \ s^{-1} \ m^{-3}]$
κ = permeability $[m^2]$
λ = thermal conductivity $[W \ m^{-1} \ K^{-1}]$
ρ = density $[kg \ m^{-3}]$
σ = Stefan–Boltzmann constant $[W \ m^{-2} \ K^{-4}]$
θ = shrinkage factor
$\dot{\omega}$ = reaction rate $[kg \ m^{-3} \ s^{-1}]$

Subscripts

ash = ash
b = bound water
char = char
$CO_{2,gasif}$ = CO_2 gasification
devol, 1 = primary devolatilization
devol, 2 = secondary devolatilization
eff = effective
evap = evaporation
g = gas phase
H_2O,g = water vapor
i = reaction
k = gas species
mix, total = mixed gas phase
oxid = char oxidation
pyro = pyrolysis
ref = reference

steam, gasif = H_2O gasification
surface = particle surface
tar = tar
wall = furnace wall
wood = dry wood
$\perp$ = perpendicular to fiber direction
∞ = bulk

Superscript

g = gas phase

■ REFERENCES

(1) Haberle, I.; Skreiberg, Ø.; Łazar, J.; Haugen, N. E. L. *Prog. Energy Combust. Sci.* **2017**, *63*, 204−252.

(2) Mehrabian, R.; Zahirovic, S.; Scharler, R.; Obernberger, I.; Kleditzsch, S.; Wirtz, S.; Scherer, V.; Lu, H.; Baxter, L. L. *Fuel Process. Technol.* **2012**, *95*, 96−108.

(3) Fatehi, H.; Bai, X. S. *Combust. Sci. Technol.* **2014**, *186*, 574−593.

(4) Lu, H.; Robert, W.; Peirce, G.; Ripa, B.; Baxter, L. L. *Energy Fuels* **2008**, *22*, 2826−2839.

(5) Porteiro, J.; Granada, E.; Collazo, J.; Patiño, D.; Morán, J. C. *Energy Fuels* **2007**, *21*, 3151−3159.

(6) Porteiro, J.; Míguez, J. L.; Granada, E.; Moran, J. C. *Fuel Process. Technol.* **2006**, *87*, 169−175.

(7) Thunman, H.; Leckner, B.; Niklasson, F.; Johnsson, F. *Combust. Flame* **2002**, *129*, 30−46.

(8) Galgano, A.; Di Blasi, C.; De Vita, R. *Energy Fuels* **2018**, *32*, 8494−8506.

(9) Sadhukhan, A. K.; Gupta, P.; Saha, R. K. *Bioresour. Technol.* **2009**, *100*, 3134−3139.

(10) Grønli, M. G. A theoretical and experimental study of the thermal degradation of biomass. Ph.D. Thesis, Norwegian University of Science and Technology, Trondheim, Norway, 1996.

(11) Strandberg, A.; Thyrel, M.; Skoglund, N.; Lestander, T. A.; Broström, M.; Backman, R. *Fuel Process. Technol.* **2018**, *176*, 211−220.

(12) Basu, P. Biomass Characteristics. In *Biomass Gasification, Pyrolysis and Torrefaction: Practical Design and Theory*, 2nd Edition; Basu, P., Ed.; Elsevier/AP: Boston, 2013; Chapter 3, pp 47−86.

(13) Pettersen, R. C. The Chemical Composition of Wood. In *The Chemistry of Solid Wood*; 1984; Chapter 2, pp 57−126.

(14) Fatehi, H. Numerical Simulation of Combustion and Gasification of Biomass Particles. Ph.D. Thesis, LTH (Lund University), Lund, Sweden, 2014.

(15) Anca-Couce, A.; Dieguez-Alonso, A.; Zobel, N.; Berger, A.; Kienzl, N.; Behrendt, F. *Energy Fuels* **2017**, *31*, 2335−2344.

(16) Burhenne, L.; Damiani, M.; Aicher, T. *Fuel* **2013**, *107*, 836−847.

(17) Link, S.; Arvelakis, S.; Hupa, M.; Yrjas, P.; Külaots, I.; Paist, A. *Energy Fuels* **2010**, *24*, 6533−6539.

(18) Weber, K.; Quicker, P. *Fuel* **2018**, *217*, 240−261.

(19) Haberle, I.; Haugen, N. E. L.; Skreiberg, Ø. *Energy Fuels* **2017**, *31*, 13743−13760.

(20) Lu, H. Experimental and modelling investigation of biomass particle combustion. Ph.D. Thesis, Brigham Young University, Provo, UT, 2006.

(21) Haberle, I.; Haugen, N. E. L.; Skreiberg, Ø. *Energy Fuels* **2018**, *32*, 6847−6862.

(22) Kim, J.-H.; Ochoa-Tapia, J. A.; Whitaker, S. *Transp. Porous Media* **1987**, *2*, 327−356.

(23) Bird, R. B.; Stewart, W. E.; Lightfoot, E. N. *Transport Phenomena*, 2nd Edition; John Wiley & Sons, Inc.: New York, 2002.

(24) Di Blasi, C. *Chem. Eng. Sci.* **1996**, *51*, 1121−1132.

(25) Hermansson, S.; Thunman, H. *Combust. Flame* **2011**, *158*, 988−999.

(26) *Wood Handbook—Wood as an Engineering Material*. General Technical Report No. FPL-GTR-190, Forest Products Laboratory; 2010.

(27) Larfeldt, J.; Leckner, B.; Melaaen, M. C. *Fuel* **2000**, *79*, 1637−1643.

(28) Wagenaar, B.; Prins, W.; van Swaaij, W. *Fuel Process. Technol.* **1993**, *36*, 291−298.

(29) Chan, W.-C. R.; Kelbon, M.; Krieger, B. B. *Fuel* **1985**, *64*, 1505−1513.

(30) Liden, A.; Berruti, F.; Scott, D. *Chem. Eng. Commun.* **1988**, *65*, 207−221.

(31) Koufopanos, C.; Papayannakos, N.; Maschio, G.; Lucchesi, A. *Can. J. Chem. Eng.* **1991**, *69*, 907−915.

(32) Di Blasi, C. *Combust. Sci. Technol.* **1993**, *90*, 315−340.

(33) Bryden, K. M.; Hagge, M. J. *Fuel* **2003**, *82*, 1633−1644.

(34) Evans, D.; Emmons, H. *Fire Saf. J.* **1977**, *1*, 57−66.

(35) Anca-Couce, A.; Sommersacher, P.; Shiehnejadhesar, A.; Mehrabian, R.; Hochenauer, C.; Scharler, R. *Energy Procedia* **2017**, *120*, 238−245.

(36) *SUNDIALS: SUite of Nonlinear and DIfferential/ALgebraic Equation Solvers - IDA*. National Laboratory Lawrence Livermore, 2016; http://computation.llnl.gov/projects/sundials/ida (accessed April 7, 2017).

(37) Biswas, A. K.; Umeki, K. *Chem. Eng. J.* **2015**, *274*, 181−191.

(38) Harada, T.; Hata, T.; Ishihara, S. *J. Wood Sci.* **1998**, *44*, 425−431.

(39) Babu, B.; Chaurasia, A. *Chem. Eng. Sci.* **2004**, *59*, 1999−2012.

(40) Alves, S.; Figueiredo, J. *Chem. Eng. Sci.* **1989**, *44*, 2861−2869.

(41) Pozzobon, V.; Salvador, S.; Bézian, J. J.; El-Hafi, M.; Le Maoult, Y.; Flamant, G. *Fuel Process. Technol.* **2014**, *128*, 319−330.